Inorganic Chemistry

Article

pubs.acs.org/IC

Periodic Trends in Lanthanide and Actinide Phosphonates: Discontinuity between Plutonium and Americium

Juan Diwu,[†] Daniel J. Grant,[‡] Shuao Wang,[†] Laura Gagliardi,[‡] and Thomas E. Albrecht-Schmitt*[,†]

[†]Department of Civil Engineering and Geological Sciences and Department of Chemistry and Biochemistry, University of Notre Dame, 156 Fitzpatrick Hall, Notre Dame, Indiana 46556, United States

[‡]Department of Chemistry and Supercomputing Institute, University of Minnesota, 207 Pleasant Street SE, Minneapolis, Minnesota 55455, United States

Supporting Information

ABSTRACT: The hydrothermal reactions of trivalent lanthanide and actinide chlorides with 1,2-methylenediphosphonic acid (**C1P2**) in the presence of NaOH or $NaNO_3$ result in the crystallization of three structure types: $RE[CH_2(PO_3H_{0.5})_2]$ (RE = La, Ce, Pr, Nd, Sm; Pu) (**A type**), $NaRE(H_2O)[CH_2(PO_3)_2]$ (RE = La, Ce, Pr, Nd, Sm, Eu, Gd, Tb, Dy; Am) (**B type**), or $NaLn[CH_2(PO_3H_{0.5})_2]\cdot(H_2O)$ (Ln = Yb and Lu) (**C type**). These crystals were analyzed using single crystal X-ray diffraction, and the structures were used directly for detailed bonding calculations. These phases form three-dimensional frameworks. In both **A** and **B**, the metal centers are found in REO_8 polyhedra as parts of edge-sharing chains or edge-sharing dimers, respectively. Polyhedron shape calculations reveal that **A** favors a D_{2d} dodecahedron while **B** adopts a C_{2v} geometry. In **C**, Yb and Lu only form isolated MO_6 octahedra. Such differences in terms of structure topology and coordination geometry are discussed in detail to reveal periodic deviations between the lanthanide and actinide series. Absorption spectra for the Pu(III) and Am(III) compounds are also reported. Electronic structure calculations with multireference methods, CASSCF, and density functional theory, DFT, reveal localization of the An 5f orbitals, but natural bond orbital and natural population analyses at the DFT level illustrate unique occupancy of the An 6d orbitals, as well as larger occupancy of the Pu 5f orbitals compared to the Am 5f orbitals.

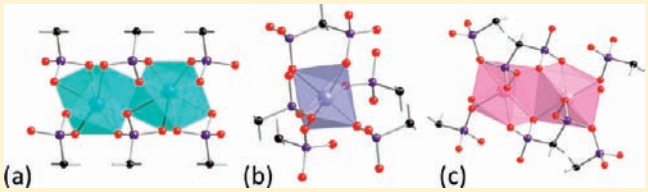

INTRODUCTION

The lanthanide series represents a unique opportunity in the periodic table to systematically study changes in structure, bonding, and reactivity as a function of the size of the metal ion without the interference of redox chemistry. The lanthanide contraction across this series represents a change of approximately 0.01 Å in ionic radius between each element, or a total change of about 0.15 Å from lanthanum to lutetium.[1] A similar trend exists in the actinide series as well, but here the behavior is considerably more complex because the early actinides are highly redox active. Several members of the series do not have trivalent oxidation states that are stable in aqueous media, especially in the presence of oxygen.[2]

However, the trivalent oxidation state becomes more stable across the actinide series in part because of the lowering of the energy of the 5f orbital, and by americium, it is the most stable oxidation state under standard conditions.[3] An additional complication is that the series cannot be fully developed because beyond californium, only microgram or submicrogram amounts of the elements have ever been available. In fact, systematic studies beyond even plutonium are rare.[4−9] What has been noted, however, is that the actinide contraction is less regular than the lanthanide contraction. For example, the reduction in the ionic radius between Pu(III) and Am(III) is large at 0.025 Å; whereas the shrinkage between Am(III) and Cm(III) is unexpectedly small at 0.005 Å.[1] These more or less pronounced changes should result in alterations in structure and bonding that either occur in different locations in the series in actinides versus lanthanides, or the transformations could, in fact, be altogether different. These ionic radii changes can also not be decoupled from the potential involvement of the 5f/6d orbitals in bonding with the actinides.

Studies on the trivalent actinide borates demonstrated that Pu(III), Am(III), and Cm(III) borates are substantially different, and often have no lanthanide analogues.[10,11] These compositional and structural deviations are indicative of multiple factors at work that encompass more than just changes in ionic radius. It was argued that the large polarizability of borate might play an important role here.[10]

In contrast to the polarizability of polyborate networks, here we provide detailed studies with a ligand that lacks such bonding, namely phosphonate, to further probe the deviation between actinides and the parallel lanthanide series. Our previous study on tetravalent lanthanide/actinide phosphonate compounds already provides evidence for the departure between transuranium elements and Ce(IV) or earlier tetravalent actinides.[12−17] Herein we demonstrate that a

Received: April 10, 2012
Published: June 5, 2012

   dx.doi.org/10.1021/ic300742p | *Inorg. Chem.* 2012, 51, 6906−6915

Table 1. Crystallographic Data for $RE[CH_2(PO_3H_{0.5})_2]$ (RE = La, Ce, Pr, Nd, Sm; Pu) (A type)

	LaC1P2	CeC1P2	PrC1P2	NdC1P2	SmC1P2	PuC1P2
formula mass	310.88	312.09	312.88	316.21	322.32	413.97
color and habit	colorless, spindle-shaped	colorless, spindle-shaped	light-pink, needle	blue-purple, spindle-shaped	colorless, spindle-shaped	light purple-blue, spindle-shaped
space group	$C2/m$ (No. 12)	$C2/m$	$C2/m$	$C2/m$	$C2/m$	$C2/m$
a (Å)	8.4055(15)	8.3514(15)	8.328(5)	8.2640(13)	8.207(2)	8.297(13)
b (Å)	14.145(3)	14.097(3)	14.080(9)	14.008(2)	13.938(4)	14.04(2)
c (Å)	5.3953(10)	5.3568(10)	5.353(3)	5.3404(8)	5.303(3)	5.335(9)
β (deg)	111.162(2)	111.342(2)	111.469(8)	111.557(2)	111.725(2)	111.498(17)
V (Å^3)	598.22(19)	587.39(19)	584.1(6)	574.97(15)	563.5(4)	578.1(16)
Z	4	4	4	4	4	4
T (K)	296(2)	296(2)	100(2)	100(2)	100(2)	100(2)
λ (Å)	0.71073	0.71073	0.71073	0.71073	0.71073	0.71073
maximum 2θ (deg.)	27.67	27.50	27.58	27.60	28.63	27.47
ρ_{calcd} (g cm^{-3})	3.452	3.529	3.558	3.653	3.799	4.757
μ(Mo $K\alpha$) (cm^{-1})	76.41	82.59	88.53	95.50	109.51	119.21
$R(F)^a$	0.0226	0.0142	0.0400	0.0192	0.0215	0.0266
$R_w(F_o^2)^b$	0.0558	0.0423	0.0806	0.0498	0.0484	0.0600

$^aR(F) = \sum||F_0| - |F_c||/\sum|F_0|$. $^bR_w(F_o^2) = [\sum[w(F_o^2 - F_c^2)^2]/\sum wF_o^4]^{1/2}$.

Table 2. Crystallographic Data for $NaRE(H_2O)[CH_2(PO_3)_2]$ (RE = La, Ce, Pr, Sm, Eu; Am) (B type)

	NaLaC1P2	NaCeC1P2	NaPrC1P2	NaSmC1P2	NaEuC1P2	NaAmC1P2
formula mass	351.88	353.08	353.88	363.32	364.92	455.97
color and habit	colorless, needle	colorless, needle	light-purple, needle	colorless, needle	colorless, needle	yellow-pink, prism
space group	$P2_1/c$ (No. 14)	$P2_1/c$	$P2_1/c$	$P2_1/c$	$P2_1/c$	$P2_1/c$
a (Å)	6.810(3)	6.757(1)	6.760(8)	6.7011(19)	6.6851(15)	6.7201(7)
b (Å)	15.159(7)	15.145(3)	15.14(2)	15.048(4)	14.998(3)	15.0851(15)
c (Å)	6.811(3)	6.764(1)	6.748(8)	6.6862(19)	6.6653(15)	6.7315(7)
β (deg)	90.914(6)	90.703(2)	90.70(1)	90.591(6)	90.522(3)	90.610(2)
V (Å^3)	703.0(6)	692.0(2)	690(1)	674.2(3)	668.3(3)	682.36(12)
Z	4	4	4	4	4	4
T (K)	298(2)	100(2)	296(2)	100(2)	100(2)	100(2)
λ (Å)	0.71073	0.71073	0.71073	0.71073	0.71073	0.71073
maximum 2θ (deg)	27.51	27.48	27.57	27.55	27.54	27.52
ρ_{calcd} (g cm^{-3})	3.325	3.370	3.405	3.580	3.607	4.439
μ(Mo $K\alpha$) (cm^{-1})	65.87	70.96	75.77	92.42	99.22	117.70
$R(F)^a$	0.0349	0.0263	0.0644	0.0222	0.0239	0.0180
$R_w(F_o^2)^b$	0.0712	0.0709	0.1528	0.0587	0.0579	0.0436

$^aR(F) = \sum||F_0| - |F_c||/\sum|F_0|$. $^bR_w(F_o^2) = [\sum[w(F_o^2 - F_c^2)^2]/\sum wF_o^4]^{1/2}$.

discontinuity exists between Pu(III) and Am(III) much like that found in borates, and additionally report the results of a computational study of their electronic structure with the aim of understanding the discontinuity and bonding.

EXPERIMENTAL SECTION

$Pu[CH_2(PO_3H_{0.5})_2]$ was synthesized using weapons-grade $PuCl_3$ (94% ^{239}Pu and 6% ^{240}Pu along with trace amounts of the other Pu isotopes and ^{241}Am). Anhydrous $PuCl_3$ that results from the recycling and electro-refining of plutonium metal was used as received. 6.2 mg (0.018 mmol) of $PuCl_3$ was placed in an autoclave in an argon-filled glovebox. 142 μL of argon-sparged water, 3.4 mg (0.019 mmol) of methylenediphosphonic acid, and 35 μL of NaOH (1M) (0.035 mmol) were added into the autoclave. The mixture was then sealed and heated at 180 °C for three days followed by cooling to room temperature in one day in the glovebox. The reaction was washed with cold water and clusters of purple-blue needle-like crystal of $Pu[CH_2(PO_3H_{0.5})_2]$ were found together with blue amorphous spheres.

$NaAm(H_2O)[CH_2(PO_3)_2]$ was synthesized using $^{243}AmO_2$ as received. 4.7 mg (0.017 mmol) of AmO_2 was dissolved in 100 μL of 5 M HCl solution (0.10 mmol) in an autoclave. The solution was dried by heating at 130 °C ending with yellow solid of hydrated $AmCl_3$. 140 μL of argon-sparged water, 2.9 mg (0.016 mmol) of methylenediphosphonic acid, and 35 μL of NaOH (1M) (0.035 mmol) were added into the autoclave consequently. However, this reaction did not yield a crystalline phase. The products were loaded back in the liner, additional 140 μL of argon-sparged water, 3.2 mg (0.018 mmol) of methylenediphosphonic acid, and 35 μL of NaOH (1M) (0.035 mmol) were added to the reaction. Crystalline products still did not form, and a third recrystallization was necessary. 140 μL of argon-sparged water, 3.0 mg (0.017 mmol) of methylenediphosphonic acid, and 50 μL of NaOH (1M) (0.050 mmol) were added to the liner to react. All three times, the reaction was heated at 180 °C for three days followed by cooling to room temperature in one day. The third reaction yielded yellow/orange crystals of $NaAm(H_2O)[CH_2(PO_3)_2]$. The crystals exhibit the Alexandrite effect and change color depending of the lighting source. They are yellow under standard illumination with fluorescence lighting in a room, but become orange under the lighting of a microscope.

dx.doi.org/10.1021/ic300742p | Inorg. Chem. 2012, 51, 6906−6915

Table 3. Crystallographic Data for $NaRE(H_2O)[CH_2(PO_3)_2]$ (RE = Nd, Gd, Tb, Dy) (B type) and $NaLu[CH_2(PO_3H_{0.5})_2]\cdot H_2O$ (C type)

	NaNdC1P2	NaGdC1P2	NaTbC1P2	NaDyC1P2	NaLuC1P2
formula Mass	357.20	370.21	371.88	375.46	455.97
color and habit	colorless, needle	colorless, needle	colorless, needle	colorless, needle	yellow-pink, prism
space group	$P2_1/c$ (No. 14)	$P2_1/c$	$P2_1/c$	$P2_1/c$	$P2_1/c$
a (Å)	6.718(3)	6.661(2)	6.677(1)	6.663(1)	6.7201(7)
b (Å)	15.056(6)	14.987(4)	15.035(3)	14.989(3)	15.0851(15)
c (Å)	6.711(3)	6.655(2)	6.657(1)	6.634(1)	6.7315(7)
β (deg)	90.650(4)	90.414(5)	90.435(2)	90.495(3)	90.610(2)
V (Å^3)	678.7(4)	664.3(5)	668.3(2)	662.5(2)	682.36(12)
Z	4	4	4	4	4
T (K)	100(2)	296(2)	296(2)	296(2)	100(2)
λ (Å)	0.71073	0.71073	0.71073	0.71073	0.71073
maximum 2θ (deg.)	27.51	27.61	27.51	27.57	27.52
ρ_{calcd} (g cm^{-3})	3.476	3.682	3.676	3.744	4.439
μ(Mo $K\alpha$) (cm^{-1})	81.78	105.23	111.18	118.20	117.70
$R(F)^a$	0.0286	0.0415	0.0279	0.0212	0.0180
$R_w(F_o^2)^b$	0.0731	0.0847	0.0737	0.0520	0.0436

$^aR(F) = \sum||F_0| - |F_c||/\sum|F_0|$. $^bR_w(F_o^2) = [\sum[w(F_o^2 - F_c^2)^2]/\sum wF_o^4]^{1/2}$.

Caution! *^{239}Pu ($t_{1/2}$ = 24,110 y) and ^{243}Am ($t_{1/2}$ = 7380 y) represent a serious health risk owing to their α and γ emission. All studies with plutonium and americium were conducted in a lab dedicated to studies on transuranium elements. This lab is equipped with a HEPA filtered hoods and negative-pressure gloveboxes. A series of counters continually monitor radiation levels in the lab. The lab is licensed by the Nuclear Regulatory Commission. All experiments were carried out with approved safety operating procedures. All free-flowing solids are worked with in gloveboxes, and products are only examined when coated with either water or Krytox oil and water.*

The $Ln[CH_2(PO_3H_{0.5})_2]$ (R = La, Ce, Pr, Nd, Sm) (**A type**), $NaLn(H_2O)[CH_2(PO_3)_2]$ (RE = La, Ce, Pr, Nd, Sm, Eu, Gd, Tb, Dy) (**B type**), and $NaLn[CH_2(PO_3H_{0.5})_2]\cdot(H_2O)$ (Ln = Yb and Lu) (**C type**) were synthesized under hydrothermal conditions as well. The detailed amounts of the starting materials are listed in Supporting Information, Table S13. All reactions were heated at 180 °C for three days followed by cooling down to room temperature in one day. Then, the crystalline products were isolated by washing with water and ethanol.

Crystallographic Studies. Crystals of all compounds were mounted on CryoLoops with Krytox oil and optically aligned on a Bruker APEXII Quazar X-ray diffractometer using a digital camera. Initial intensity measurements were performed using a IμS X-ray source, a 30 W microfocused sealed tube (MoKα, λ = 0.71073 Å) with high-brilliance and high-performance focusing Quazar multilayer optics. Standard APEXII software was used for determination of the unit cells and data collection control. The intensities of reflections of a sphere were collected by a combination of four sets of exposures (frames). Each set had a different φ angle for the crystal, and each exposure covered a range of 0.5° in ω. A total of 1464 frames were collected with an exposure time per frame of 10 to 50 s, depending on the crystal. SAINT software was used for data integration including Lorentz and polarization corrections.[18,19] Selected crystallographic information is listed in Tables 1−3. Atomic coordinates and additional structural information are provided in the Supporting Information (CIF's).

UV−vis−NIR Spectroscopy. UV−vis−NIR data were acquired from single crystals using a Craic Technologies microspectrophotometer. Pu(III) and Am(III) crystals were placed on quartz slides under oil, and the data was collected from 250 to 1400 nm.

■ COMPUTATIONAL METHODS

Quantum chemical calculations were performed using density functional theory (DFT)[20,21] and multiconfigurational methods (CASSCF)[22,23] with the aim of investigating the electronic structure of the Pu^{3+} and Am^{3+} phosphonates. The initial structures were obtained from the available experimental crystal structures of $Pu[CH_2(PO_3H_{0.5})_2]$, **PuC1P2**, and $NaAm(H_2O)[CH_2(PO_3)_2]$, **AmC1P2**. The models employed to represent each crystal structure were constructed to include two An^{3+} metal sites and the immediate coordinating methylenedisphonate $[CH_2(PO_3)_2]$ ligands. However, to make the models more computationally feasible, for both **PuC1P2** and **AmC1P2**, the PO_3 groups not coordinated to the actinide metal were replaced by hydrogen atoms to give $[CH_3(PO_3)]$ ligands. Additionally, to further reduce the overall negative molecular charge of the constructed models, terminal oxygen atoms of the PO_3 groups not directly bonded to the actinide metal were also protonated. The coordinates of both **PuC1P2** and **AmC1P2** models employed in the calculations are reported in the Supporting Information, Table SI 4 as *XYZ* coordinates. Constrained geometry optimizations of the protons (H^+) were consequently performed on the constructed models where the actinide metal and phosphonate framework were kept frozen at the geometry of the experimental crystal structure.

The constrained geometry optimizations were performed at the DFT level with the Perdew−Burke−Ernzerhof (PBE) exchange-correlation functional[24] and a triple-ζ valence plus polarization (def-TZVP)[25] basis set on all atoms. Quasi-relativistic pseudopotentials were used for the Pu and Am atoms with a core of 60 electrons, respectively.[25,26] The constrained geometry optimizations were performed at an energy convergence of $\Delta E_h = 10^{-6}$ and a grid size of m = 5. All DFT calculations were performed with the TURBOMOLE 5.10 program package.[25,27]

Single-point multiconfigurational complete active space (CASSCF)[16] calculations were performed at the DFT optimized geometries. Scalar relativistic effects were included using the Douglas−Kroll−Hess[28] Hamiltonian to second-order and the relativistic all electron ANO-RCC basis sets with double-ζ quality (ANO-RCC-VDZP)[29] with the following contractions: [8s7p5d3f1g] for Pu and Am and [3s2p1d] for O. The ANO-RCC-MB basis set was employed for P, Na, C, and H with contractions of [3s2p], [3s2p], [2s1p], and [1s], respectively. CASSCF calculations on the An^{3+} phosphonate complexes were performed at the optimized PBE/def-TZVP geometries. The ground state electronic configuration was slightly complex because of the unpaired f-electrons per actinide atom in **PuC1P2** and **AmC1P2** of Pu $5f^5$ and Am $5f^6$, respectively. The initial active spaces for **PuC1P2** and **AmC1P2** included 10 and 12 electrons in 14 An 5f-orbitals, respectively. The final active space was expanded to include an additional doubly occupied orbital and the corresponding antibonding orbital, and for both **PuC1P2** and **AmC1P2**, the additional orbital was an An 6p.

dx.doi.org/10.1021/ic300742p | Inorg. Chem. 2012, 51, 6906−6915

Table 4. Selected Bond Distances (Å) for RE[$CH_2(PO_3H_{0.5})_2$] (RE = La, Ce, Pr, Nd, Sm; Pu) (A type)

bond distances (Å)	La	Ce	Pr	Nd	Sm	Pu
M(1)−O(1)×2	2.630(4)	2.613(2)	2.587(6)	2.550(3)	2.524(3)	2.582(7)
M(1)−O(2)×2	2.483(3)	2.460(2)	2.455(5)	2.430(3)	2.411(3)	2.434(6)
M(1)−O(2)×2	2.583(3)	2.562(2)	2.546(5)	2.533(3)	2.507(3)	2.544(6)
M(1)−O(3)×2	2.412(4)	2.383(2)	2.377(5)	2.351(3)	2.319(4)	2.369(6)
P(1)−O(1)	1.566(3)	1.557(2)	1.568(6)	1.570(3)	1.569(3)	1.557(6)
P(1)−O(2)	1.530(4)	1.531(2)	1.539(6)	1.531(3)	1.519(3)	1.530(6)
P(1)−O(3)	1.504(4)	1.497(2)	1.510(6)	1.508(3)	1.508(4)	1.507(6)
P(1)−C(1)	1.795(4)	1.791(2)	1.794(6)	1.796(3)	1.795(3)	1.798(7)
Average(M−O)	2.528(4)	2.504(2)	2.491(6)	2.466(3)	2.440(4)	2.482(7)

The computational costs arising from the two-electron integrals were drastically reduced by employing the Cholesky decomposition (CD) technique in all CASPT2 calculations[30−32] combined with the Local Exchange (LK) screening.[33] The CASPT2 approach has been successful in studying many actinide-containing systems.[34−38] The CASSCF/CASPT2 calculations were performed with the MOLCAS 7.3 package.[39]

RESULTS AND DISCUSSION

Synthesis. The hydrothermal reactions of $LnCl_3$ (Ln = La, Ce, Pr, Nd, Sm, Eu, Gd, Tb, Dy, Ho, Tm, Yb, Lu) or $AnCl_3$ (An = Pu, Am) with methylenediphosphonic acid (C1P2) and 1 M NaOH solution or $NaNO_3$ results in the formation of crystals of Ln[$CH_2(PO_3H_{0.5})_2$] (Ln = La, Ce, Pr, Nd, Sm) (**A type**), NaLn(H_2O)[$CH_2(PO_3)_2$] (RE = La, Ce, Pr, Nd, Sm, Eu, Gd, Tb, Dy) (**B type**), or NaLn[$CH_2(PO_3H_{0.5})_2$]·(H_2O) (Q = Yb and Lu) (**C type**) as the only crystalline phase of each reaction. The early lanthanide compounds were isolated from the reactions with NaOH. Moving to the heavier lanthanide elements, there is a trend of decreasing solubility as the atomic number increases.[40] As a consequence, using NaOH only results in an amorphous powder, possibly the lanthanide hydroxide. By switching to $NaNO_3$, we were able to assemble the late lanthanide series. Although Na^+ is not incorporated into the **A** type structure, it is observed to play a critical role in the growth of these crystalline phases. The Na^+ concentration in the reactions that yielded lanthanide crystals has an extremely narrow range, especially in the late lanthanide series.

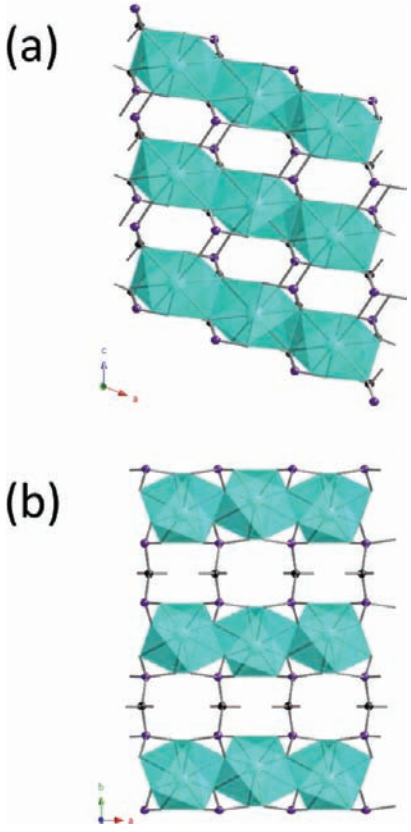

Figure 1. Depiction of three-dimensional framework structures of α-R[$CH_2(PO_3H_{0.5})_2$] (R = La, Ce, Pr, Nd, Sm; Pu): (a) the view down the *b* axis showing the pseudolayer, (b) the view down the *c* axis showing the CH_2 linking the layers together. Color code: R (RE = La, Ce, Pr, Nd, Sm; Pu), blue polyhedron; phosphorus, purple; carbon, black.

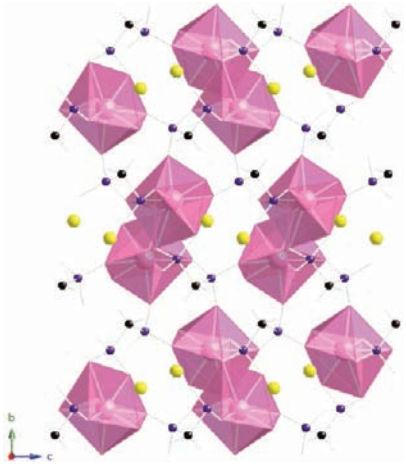

Figure 2. Depiction of three-dimensional framework structures of NaRE(H_2O)[$CH_2(PO_3)_2$] RE (RE = La−Tm; Am) from the (001) direction. The RE (RE = La−Tm; Am) dimer is pink, phosphorus in purple, carbon in black, and sodium in yellow.

Table 5. Selected Bond Distances (Å) for NaRE(H_2O)[$CH_2(PO_3)_2$] (RE = La, Ce, Pr, Sm, Eu; Am) (B type)

Q−O distances (Å)	La	Ce	Pr	Nd	Sm
(1)M−O	2.417(4)	2.359(4)	2.399(11)	2.401(4)	2.385(3)
(1)M−O	2.397(4)	2.423(4)	2.372(11)	2.338(4)	2.308(3)
(1)M−O	2.454(5)	2.431(4)	2.421(11)	2.402(4)	2.378(3)
(1)M−O	2.457(4)	2.438(4)	2.430(9)	2.403(4)	2.382(3)
(1)M−O	2.561(4)	2.513(4)	2.609(12)	2.574(4)	2.565(3)
(1)M−O	2.561(4)	2.552(4)	2.510(11)	2.508(4)	2.467(3)
(1)M−O	2.626(5)	2.613(4)	2.527(10)	2.508(4)	2.481(3)
(1)M−O	2.723(5)	2.684(4)	2.681(14)	2.641(4)	2.617(4)
Average	2.524(5)	2.501(4)	2.494(12)	2.472(4)	2.448(3)

dx.doi.org/10.1021/ic300742p | *Inorg. Chem.* 2012, 51, 6906−6915

Table 6. Selected Bond Distances (Å) for $NaRE(H_2O)[CH_2(PO_3)_2]$ (RE = Nd, Gd, Tb, Dy) (B type)

Q–O Distances (Å)	Eu	Gd	Tb	Dy	Am
(1)M–O	2.374(5)	2.359(6)	2.350(4)	2.334(3)	2.408(4)
(1)M–O	2.286(4)	2.280(6)	2.261(4)	2.246(3)	2.339(4)
(1)M–O	2.367(4)	2.368(5)	2.355(4)	2.339(3)	2.415(4)
(1)M–O	2.370(4)	2.352(6)	2.356(4)	2.341(3)	2.404(4)
(1)M–O	2.549(4)	2.544(6)	2.555(4)	2.541(3)	2.587(4)
(1)M–O	2.446(4)	2.444(7)	2.429(4)	2.419(3)	2.489(4)
(1)M–O	2.462(4)	2.463(6)	2.453(4)	2.435(3)	2.513(4)
(1)M–O	2.621(4)	2.601(6)	2.609(5)	2.593(3)	2.649(4)
Average	2.434(5)	2.426(7)	2.421(4)	2.406(3)	2.476(4)

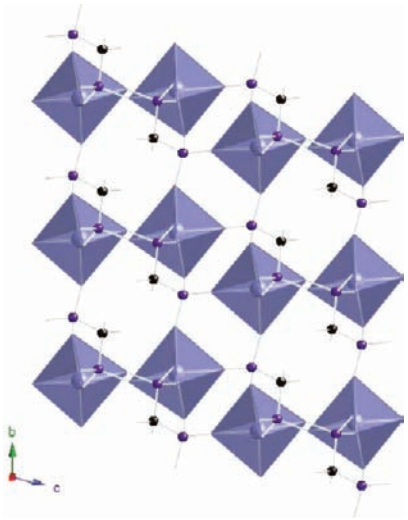

Figure 3. Depiction of three-dimensional framework structures of $Q[CH_2(PO_3)_2]\cdot 3(H_2O)$ (Q = Yb, Lu). The Q (Q = Yb, Lu) dimer is dark blue, phosphorus in purple, carbon in black. The water molecules in the cavities are omitted for clarity.

Table 7. Selected Bond Distances (Å) for $NaLu[CH_2(PO_3H_{0.5})_2]\cdot(H_2O)$ (C type)

bond distances (Å)	Lu
Lu(1)–O(1)	2.229(5)
Lu(1)–O(2)	2.199(5)
Lu(1)–O(3)	2.181(4)
Lu(1)–O(4)	2.206(4)
Lu(1)–O(5)	2.219(4)
Lu(1)–O(6)	2.212(4)
Average	2.208(5)

Each element yields crystals from different amounts of Na^+ compared with the adjacent elements.

Crystal Structure Descriptions. All three structures are substantially different in terms of structure topology, coordination number, and metal polyhedron geometry. The structure of $RE[CH_2(PO_3H_{0.5})_2]$ (RE = La, Ce, Pr, Nd, Sm; Pu) (**A type**) is a three-dimensional framework where the metal polyhedra are edge-sharing chains that are further connected by the ligand C1P2. The shape of the polyhedron was calculated by Shape8 measurements to be a D_{2d} dodecahedron (Supporting Information, Table SI 4). The structure of $NaRE(H_2O)[CH_2(PO_3)_2]$ (RE= La, Ce, Pr, Nd, Sm, Eu, Gd, Tb, Dy; Am) (**B type**) is also a three-dimensional framework structure. The basic building unit of this structure is an edge-sharing dimer. These dimers are linked by C1P2 and extend in all three directions. Shape8 calculations show that this polyhedron possesses C_{2v} symmetry (Supporting Information, Table SI 5). The structure of $NaLn[CH_2(PO_3H_{0.5})_2]\cdot(H_2O)$ (Ln = Yb, Lu) (**C type**) is another three-dimensional framework where the metal polyhedra are isolated monomers. The metal centers here are six-coordinate compared to the previous eight-coordinate metal centers.

Crystal Structure of $RE[CH_2(PO_3H_{0.5})_2]$ (RE = La, Ce, Pr, Nd, Sm; Pu) (A type). This is a three-dimensional framework structure where the metal polyhedra are edge-sharing chains that are further connected by the ligand C1P2. Detailed bond distances for each compound are listed in Table 4. The shape of the polyhedra is calculated by Shape8 measurements to be a D_{2d} dodecahedron (Supporting Information, Table SI 4). The two PO_3 groups in the C1P2 bond to the metal centers in the same manner. O1 from one of the PO_3 moieties bridges between the phosphorus center and the rare earth metal ion. In contrast, O2 is a μ_3-oxo atom that bonds to both this metal center and an adjacent one thus connecting all polyhedra together to form edge-sharing chains (Figure 1a). O3 further bonds to a metal center of a second chain and forms pseudo layers by connecting all the chains together. Bond-valence sum calculation suggests that the third oxygen atom is actually partially protonated (Supporting Information, Table SI 6). Furthermore, the pseudo layers are connected by the CH_2 moiety that joins the two PO_3 groups together to form an extended three-dimensional framework structure (Figure 1b).

Crystal Structure of $NaRE(H_2O)[CH_2(PO_3)_2]$ (RE = La, Ce, Pr, Nd, Sm, Eu, Gd, Tb, Dy; Am) (B type). **B** is also a three-dimensional framework structure as shown in Figure 2. The basic building unit of this structure is an edge-sharing dimer. Detailed bond distances for each compound are listed in Tables 5 and 6. These dimers are linked by the C1P2 unit and extend in all three directions. One of the PO_3 units in C1P2 chelates one metal center using two oxo atoms, and bridges the second metal center by a μ_3-O. The third oxo atom of this PO_3 unit is bound to an adjacent metal center of the dimer. The second PO_3 unit does not chelate a metal center, but bridges three metal centers from different dimers. As a result, these dimers are linked together into a three-dimensional network. Shape8 calculations show that this polyhedron adopts C_{2v} symmetry (Supporting Information, Table SI 5). There are seven oxo atoms that bond to the metal center with the eighth one occupied by water. One Na^+ cation is found in the void space within the framework to maintain charge balance. As a result, all the oxygen atoms from the C1P2 ligand are fully deprotonated. BVS calculations results are listed in Supporting Information, Table S4.

Crystal Structure of $NaLn[CH_2(PO_3H_{0.5})_2]\cdot(H_2O)$ (Ln = Yb, Lu) (C type). **C** is another three-dimensional framework where the metal polyhedra are isolated monomers shown in Figure 3. The metal centers here are six-coordinate compared to the previous all eight-coordinate compounds (Table 7). All six oxygen atoms are from the C1P2 ligand, which are all deprotonated as indicated by the BVS calculations listed in Supporting Information, Table SI 7. Two of them are from the same C1P2 unit, which chelate the metal center in this manner. The other four are all from adjacent C1P2 units that are bound to the metal centers to extend the structure into a three-dimensional framework. The bond distances show an obvious contraction (Table 6). The cavity size in this structure type is

dx.doi.org/10.1021/ic300742p | Inorg. Chem. 2012, 51, 6906–6915

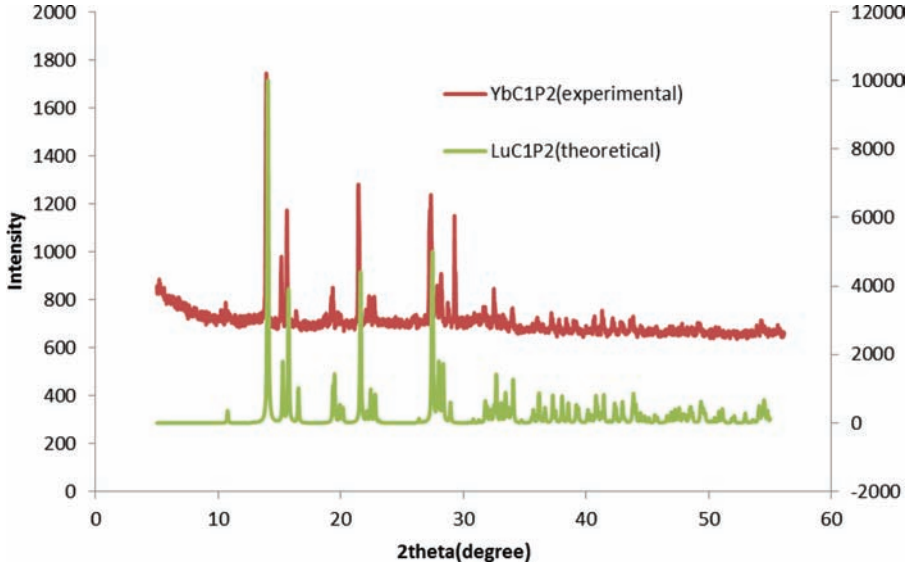

Figure 4. Experimental powder XRD pattern of the Yb crystals (red) compared to the theoretical powder XRD pattern of $Lu[CH_2(PO_3)_2]\cdot 3(H_2O)$ generated from the single crystal XRD data. The Yb crystal should adopt the same structure as the $Lu[CH_2(PO_3)_2]\cdot 3(H_2O)$.

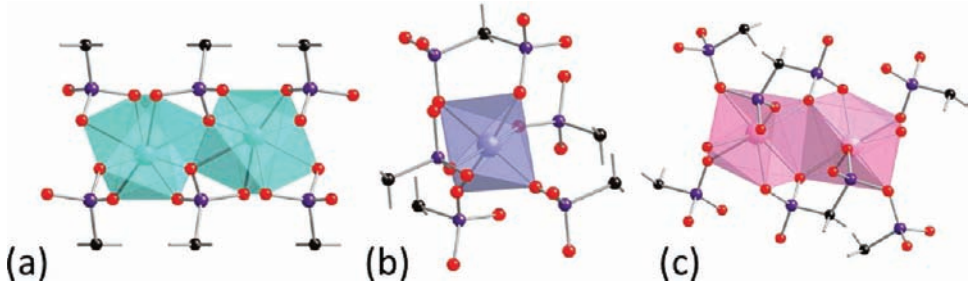

Figure 5. Detailed view of the coordination environments of the three structure types. (a) α-$R[CH_2(PO_3H_{0.5})_2]$ (RE = La, Ce, Pr, Nd, Sm; Pu). (b) β-$Q[CH_2(PO_3)_2]\cdot 3(H_2O)$ (Q = Yb, Lu), (c) $NaRE(H_2O)[CH_2(PO_3)_2]$ RE (RE = La–Tm; Am). The metal center polyhedra are shown in light blue, dark blue, and pink, respectively. The phosphorus is purple, carbon in black, and oxygen in red.

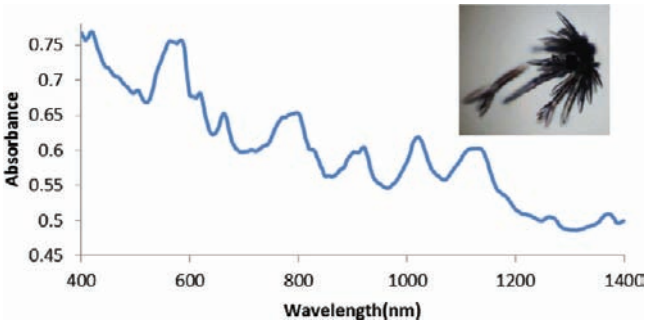

Figure 6. UV–vis–NIR absorption spectrum of $Pu[CH_2(PO_3H_{0.5})_2]$ showing the fingerprint peaks for Pu(III) and the picture of the crystals.

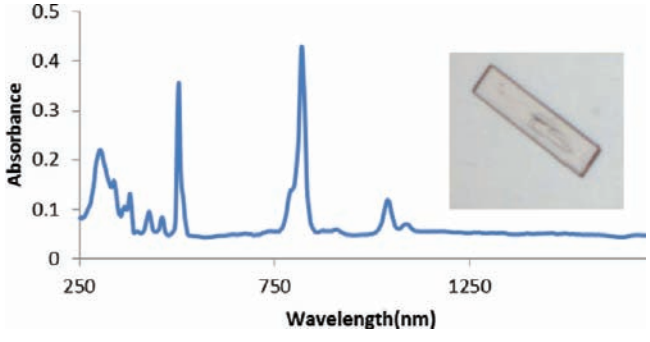

Figure 7. UV–vis–NIR absorption spectrum of $NaAm(H_2O)[CH_2(PO_3)_2]$ showing the fingerprint peaks for Am(III) and the picture of the crystals.

larger than the **B** type. There are Na^+ cations and H_2O molecules disordered in the cavity. Crystals with Yb(III) were too small for single crystal XRD. However, powder XRD shows that the pattern of the Yb(III) compared is essentially identical to the calculated powder pattern of the Lu(III) indicating that these two should have the same structure type as shown in Figure 4.

Structural Comparisons of A, B, and C Types. Even though all three structures adopt three-dimensional frameworks, their topologies are different. As mentioned above, in **A**, the metal centers form edge-sharing chains that further link to each other by the C1P2 ligand to extend in three dimensions. In **B**, the building unit is edge-sharing dimers that are linked together by the ligand. In the **C** type structure, the topology only contains monomers. In addition, the bonding mode of the ligand differs. In all three phases, the C1P2 ligand chelates the metal centers. However, a closer look at the bonding on the PO_3 groups show that, in **A**, the two PO_3 unit both chelate the metal centers, while in the Na phase, only one does. In **B**, neither of the PO_3 moieties chelates the metal center. Further comparison reveals that, with the addition of sodium cations in

dx.doi.org/10.1021/ic300742p | Inorg. Chem. 2012, 51, 6906–6915

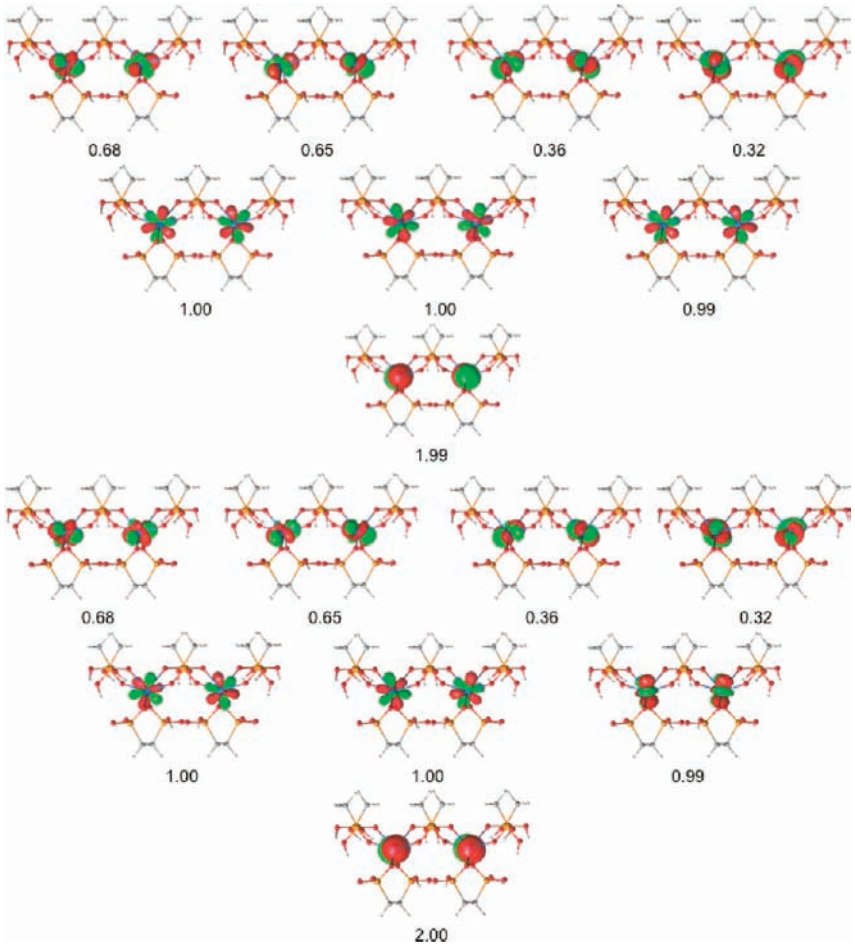

Figure 8. CASSCF molecular orbitals responsible for the bonding in **PuC1P2** for a (14, 16) active space. Respective occupation numbers are indicated below the orbital plots (isovalue 0.04). Pu, blue; P, orange; O, red; C, gray; and H, white.

B and **C**, the protonation of the ligand differs. In **A**, the PO_3 groups are half deprotonated to balance the charge while in **B** and **C** they are fully deprotonated. Additionally, it is noteworthy that the content of the cavities changes. **A** has no other ions in the cavity, while in **B**, we find Na^+ in the cavity. **C** is able to adopt both Na^+ ions and water molecules in the cavity.

The coordination environments of the metal centers in the three phases diverge from each other (Figure 5). As mentioned above, the coordination number in **C** type is six (Table 7), while the metal centers are eight-coordinate in the other two phases. However, Shape8 calculations of the eight-coordinate **A** and **B** type structures show that although the coordination numbers are the same, the geometry still differs from one another. In **A**, the metal center is a D_{2d} dodecahedron while in **B** it is C_{2v}. The possible explanation of this is the involvement of water in bonding in **B**, which forms a much longer bond compared to the typical RE-O-P bonds, and thus further lowers the symmetry.

As we have observed from the above data, the structures of lanthanide methylenediphosphonates (Ln = La, Ce, Pr, Nd, Sm, Eu, Gd, Tb, Dy) are not all isotypic, but rather a structural transformation takes place across the series. The lanthanum, cerium, neodymium, and samarium compounds are isotypic. The **B** type structure is adopted by most of the lanthanides from La to Dy. Yb and Lu present the **C** type structure, which is inconsistent with other lanthanides. Experiments with lanthanides smaller than europium fail to yield crystalline materials with NaOH, possibly because we are dealing with a higher hydrolysis constant. The success of making those compounds is achieved by replacing NaOH with $NaNO_3$. While there is not a direct match in ionic radius between Pu(III) and any lanthanide, the closest match is with La(III), and, in fact, $Pu[CH_2(PO_3H_{0.5})_2]$ is isotypic with $Ln[CH_2(PO_3H_{0.5})_2]$ (Ln = La, Ce, Pr, Nd, Sm). The smaller Am(III) cation, however, does not adopt this structure type, but rather occurs as $NaAm(H_2O)[CH_2(PO_3)_2]$, which is isotypic with $NaLn(H_2O)[CH_2(PO_3)_2]$ (Ln = La, Ce, Pr, Nd, Sm, Eu, Gd, Tb, Dy).

It is noteworthy that attempts to crystallize Cm(III) crystals failed under these same conditions. The synthetic difference between the two phases is the amount of NaOH or $NaNO_3$ that was used in the reactions. With a relatively smaller amount of Na^+, **A** type crystal forms, from La to Sm and for Pu. A slight increase in Na^+ yields **B** type compounds for Ln(III) and Am(III). For the Pu(III) and Am(III) reactions, both reactions were tried with low and high Na^+ amount; however, Pu(III) only forms **A**, while Am(III) only forms **B**.

UV−vis−NIR Spectroscopy. The UV−vis−NIR spectra of Pu(III) and Am(III) compounds are shown in Figures 6 and 7 along with pictures of the crystals. The absorption spectrum of $Pu[CH_2(PO_3H_{0.5})_2]$ shows the fingerprint peaks of Pu(III) at 580 ($^4M_{15/2}$), 650 ($^4L_{13/2}$), 800 ($^6H_{15/2}$), 900 ($^6H_{13/2}$), 1000 ($^6H_{13/2}$), and 1150 nm ($^6H_{11/2}$).[21] The $NaAm[CH_2(PO_3)_2]$

dx.doi.org/10.1021/ic300742p | Inorg. Chem. 2012, 51, 6906−6915

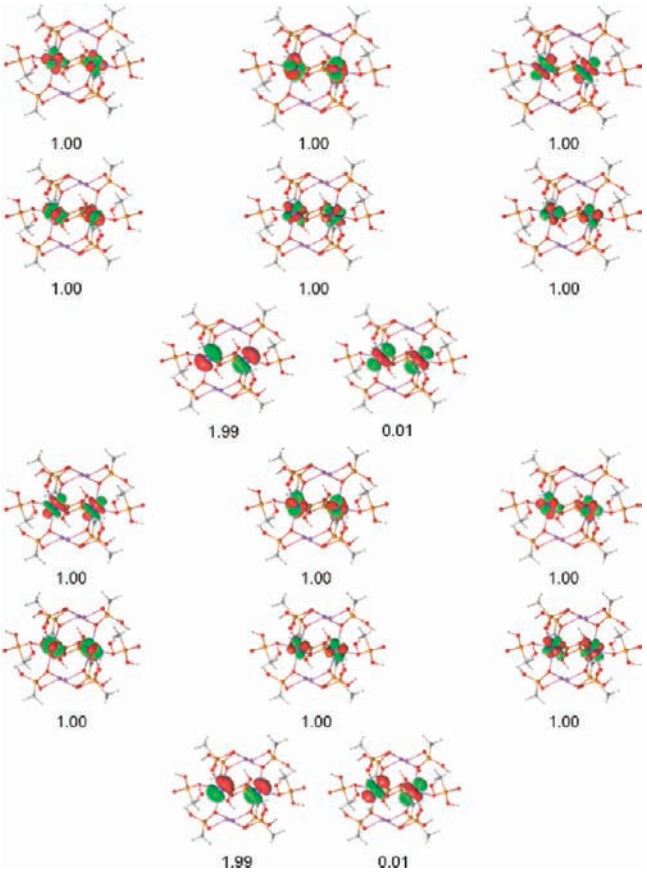

Figure 9. CASSCF molecular orbitals responsible for the bonding in **AmC1P2** for a (16, 16) active space. Respective occupation numbers are indicated below the orbital plots (isovalue 0.04). Am, blue; Na, purple; P, orange; O, red; C, gray; and H, white.

spectrum contains characteristic peaks at 500 ($^5L_6$), 820 ($^7F_6$), and 1050 nm ($^7F_4$) indicating the trivalent state of Am (Figure 7).[41,42]

Electronic Structure Calculations. Insights into the involvement of the 5f orbitals in bonding were obtained through electronic structure analyses of **PuC1P2** and **AmC1P2** at the CASSCF level, respectively. Selected molecular orbitals in the HOMO−LUMO region involving the 5f orbitals are depicted in Figures 8 and 9, respectively.

The active space for **PuC1P2** and **AmC1P2** included 10 and 12 electrons in 14 An 5f orbitals and an additional doubly occupied orbital pair, respectively. Irrespective of structure and actinide metal, the An 5f orbitals are localized on the metal site (Figures 8 and 9), respectively. There is no evident interaction of the An 5f orbitals with any coordinating oxygen atoms of the phosphonate ligands. Expanding the active space below the valence 5f orbitals introduces an An 6p orbital in both **PuC1P2** and **AmC1P2**, which also shows no interaction with the coordinating ligands (Figure 8 and 9).

Additional electronic structure analyses were performed at the PBE/def-TZVP level. The highest singly occupied α spin orbitals (SOMOs) are depicted in Figures 10 and 11. For **PuC1P2** and **AmC1P2**, the 10 and 12 highest SOMOs are localized An 5f orbitals. In both cases, there is a little electron density delocalized on the O 2p orbital of select coordinating PO_3 groups. Moreover, just below the localized valence An 5f orbitals are O 2p orbitals of the coordinating PO_3 groups.

Further insights into the electronic structure of these An^{3+} phosphonate complexes were obtained from natural bond orbital (NBO) and natural population (NPA) analyses. At the CASSCF level, the Mülliken and LoProp methods predict similar partial atomic charges for the actinide metal in **PuC1P2** and **AmC1P2** (Table 8). However, the Mülliken charges were predicted to be on average 0.4e larger than the LoProp charges and closer to the trivalent oxidation state. Similarly, the atomic partial charges were predicted at the DFT level, where the Mülliken and NPA atomic charges (Table 8) were even further away from ideal +3 value than the predicted CASSCF charges. The natural charge on Pu was predicted to be less than that of Am by ~0.2e, indicating a larger transfer of electron density from the coordinating oxygen atoms of the PO_3 groups to the actinide metal in **PuC1P2** than in **AmC1P2**.

Furthermore, the NPA electronic configurations also reveal a unique involvement of the An 6d orbitals. From NPA calculations, the electronic configurations of Pu $6d^{0.79}$ vs Am $6d^{0.84}$ reveals electron occupation for Am 6d to be larger, while at the Mülliken level, the situation is marginally reversed, and the orbital occupation of the Pu 6d orbital is slightly larger, Pu $6d^{0.54}$ vs Am $6d^{0.51}$ (Supporting Information, Table SI 1).

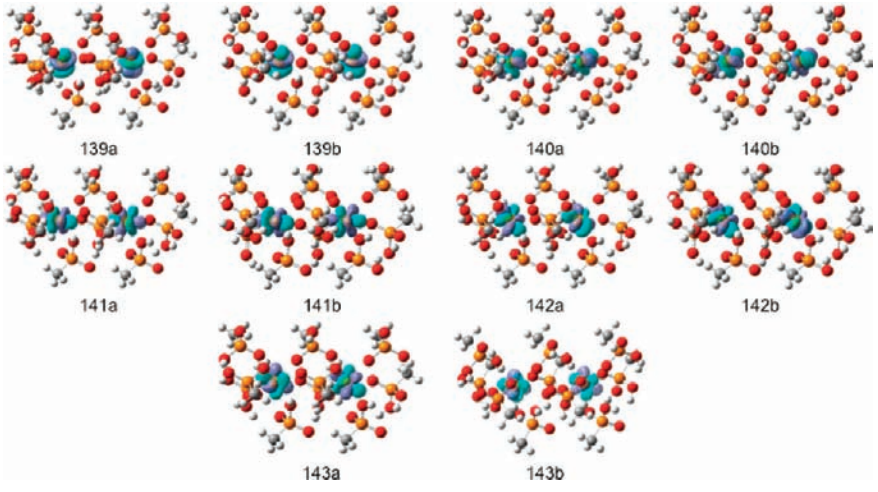

Figure 10. Singly occupied α spin orbital plots involving the Pu 5f orbital in **PuC1P2** at the DFT-PBE level (isovalue 0.04). Pu, orange-yellow; P, orange; O, red; C, gray; and H, white.

dx.doi.org/10.1021/ic300742p | *Inorg. Chem.* 2012, 51, 6906−6915

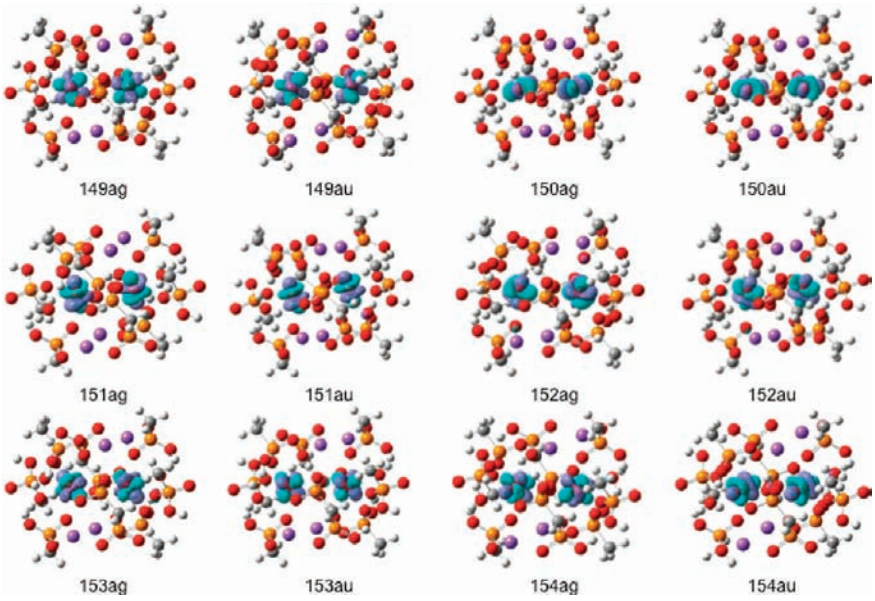

Figure 11. Singly occupied α spin orbital plots involving the Am 5f orbital in **AmC1P2** at the DFT-PBE level (isovalue 0.04). Am, burgundy; P, orange; O, red; C, gray; and H, white.

Table 8. Partial Atomic Charges Per Actinide Metal in PuC1P2 and AmC1P2 at the CASSCF/ANO-RCC-PVDZ and DFT-PBE/def-TZVP Levels

	CASSCF		DFT	
molecule	Mülliken	LoProp	Mülliken	natural population analysis
PuC1P2	2.87	2.45	1.10	1.57
AmC1P2	2.86	2.49	1.44	1.71

Table 9. Atomic Populations from the Total Density in PuC1P2 and AmC1P2 at the DFT-PBE/def-TZVP Level

method	An	6s	6p	5d	5f
Loewdin	Pu	4.185	12.440	11.467	5.895
	Am	4.158	12.435	11.483	6.682
natural population analysis	Pu	4.165	11.994	10.844	5.423
	Am	4.164	11.990	10.888	6.246
Mülliken	Pu	4.267	12.301	10.906	5.404
	Am	4.215	12.183	10.822	6.320

Table 10. Total ($\alpha-\beta$) Spin Density in PuC1P2 and AmC1P2 at the DFT-PBE/def-TZVP Level

method	An	6s	6p	5d	5f	total
Loewdin	Pu	0.009	0.023	0.072	4.927	5.030
	Am	0.010	0.025	0.074	5.916	6.026
natural population analysis	Pu	0.017	0.062	0.101	4.915	5.096
	Am	0.020	0.070	0.108	5.903	6.101
Mülliken	Pu	0.023	0.015	0.079	4.949	5.066
	Am	0.029	0.012	0.085	5.935	6.061

However, irrespective of method, there is electron occupation of the An 6d orbitals. Considering the atomic orbital occupations of the An5f orbitals, Pu $5f^{5.38}$ vs Am $5f^{6.23}$, shows more electron occupation for Pu, indicating a larger transfer of electron density to this metal site. A similar observation is predicted by the Mülliken method, Pu $5f^{5.04}$ vs Am $5f^{6.03}$ (Supporting Information, Table SI 1). This is consistent with the ionic contraction in going from Pu^{3+} to Am^{3+}, and the expected localization and decreased involvement of the An 5f orbital.

Atomic populations from the total density were also predicted at the DFT level from NPA, Mülliken, and Loewdin methods (Table 9). In general, the Loewdin atomic populations were slightly larger in value than both Mülliken and NPA. However, irrespective of method, the atomic populations on the actinide metal in **PuC1P2** than **AmC1P2** are approximately the same, except for the An 5f orbital. Additionally, irrespective of method, the atomic populations indicated an increased occupancy of the An 6p and An 5d orbitals beyond the expected An $6p^6$ and An $5d^{10}$, illustrating a transfer of electrons from the coordinating oxygen atoms (Table 9). The Pu 5d orbital population was slightly lower at the Loewdin and NPA levels, while the situation is reversed at the Mülliken method. Considering the An 5f orbitals, each method predicted a comparative increase in atomic population for Pu 5f compared to Am 6f.

Lastly, the total and decomposed atomic ($\alpha-\beta$) spin density is considered (Table 10), and irrespective of method, the total ($\alpha-\beta$) spin density are as expected for each metal (Pu ~5 and Am ~6) with the largest contribution coming from the An 5f orbital. Population analysis based on occupation numbers indicated the sharing of electrons between the actinide metals and the immediate coordinating O atoms, as well as the nearest coordinating P atoms of the phosphonate ligands (Supporting Information, Table SI 2 and 3). Furthermore, there is the sharing of electron density between the actinide metals with that of Am−Am being 0.26*e* and Pu−Pu 0.11*e*.

CONCLUSIONS

In this lanthanide and actinide phosphonate system, we have prepared three different structure types, which demonstrate that different compounds form as a function of the size of the metal ions and perhaps other factors in the actinide series. The early lanthanides are able to adopt both **A** and **B** structure types, whereas Pu(III) only forms **A** and Am(III) only crystallizes in **B**. This discontinuity between Pu(III) and Am(III) parallels that found in borate even though

dx.doi.org/10.1021/ic300742p | *Inorg. Chem.* 2012, 51, 6906−6915

phosphonates are not highly polarizable ligands. Electronic structure calculations at the CASSCF and DFT levels reveal localization of the An 5f orbitals, but natural bond orbital and natural population analyses at the DFT level illustrate unique occupancy of the An 6d orbitals and larger relative occupancy of the Pu 5f compared to the Am 5f orbitals.

■ ASSOCIATED CONTENT

Supporting Information

X-ray crystallographic files for all the crystal structures in CIF format, and the bonding details, BVS calculation, and SEM-EDS results (PDF). This material is available free of charge via the Internet at http://pubs.acs.org.

■ AUTHOR INFORMATION

Corresponding Author

*E-mail: talbrec1@nd.edu.

Notes

The authors declare no competing financial interest.

■ ACKNOWLEDGMENTS

We are grateful for support provided by the Chemical Sciences, Geosciences, and Biosciences Division, Office of Basic Energy Sciences, Office of Science, Heavy Elements Chemistry Program, U.S. Department of Energy, under Grant DE-FG02-09ER16026.

■ REFERENCES

(1) Shannon, R. D. *Acta Crystallogr.* **1976**, *A32*, 751−767.
(2) (a) Sullivan, J. C.; Gordon, S.; Mulac, W. A.; Schmidt, K. H.; Cohen, D.; Sjoblom, R. *Inorg. Nucl. Chem. Lett.* **1976**, *12*, 599−601. (b) Sullivan, J. C.; Gordon, S.; Mulac, W. A.; Sjoblom, R. *J. Phys. Chem.* **1976**, *80*, 1684−1686. (c) Gordon, S.; Mulac, W.; Schmidt, K. H.; Sjoblom, R. K.; Sullivan, J. C. *Inorg. Chem.* **1978**, *17*, 294−296.
(3) Edelstein, N. M.; Fuger, J.; Katz, J. J.; Morss, L. R. In *The Chemistry of the Actinide and Transactinide Elements*; Morss, L. R., Edelstein, N. M., Fuger, J., Eds.; Springer: Dordrecht, The Netherlands, 2006; Vol. 3, Chapter 15, p 1776.
(4) (a) Burns, J. H.; Peterson, J. R. *Acta Crystallogr.* **1970**, *B26*, 1885−1887. (b) Burns, J. H.; Peterson, J. R.; Stevenson, J. N. *J. Inorg. Nucl. Chem.* **1975**, *37*, 743−749.
(5) (a) Matonic, J. H.; Scott, B. L.; Neu, M. P. *Inorg. Chem.* **2001**, *40*, 2638−2639. (b) Lindqvist-Reis, P.; Apostolidis, C.; Rebizant, J.; Morgenstern, A.; Klenze, R.; Walter, O.; Fanghaenel, T.; Haire, R. G. *Angew. Chem., Int. Ed.* **2007**, *46*, 919−922. (c) Apostolidis, C.; Schimmelpfennig, B.; Magnani, N.; Lindqvist-Reis, P.; Walter, O.; Sykora, R.; Morgenstern, A.; Colineau, E.; Caciuffo, R.; Klenze, R.; Haire, R. G.; Rebizant, J.; Bruchertseifer, F.; Fanghanel, T. *Angew. Chem., Int. Ed.* **2010**, *49*, 6343−6347.
(6) (a) Peterson, J. R.; Burns, J. H. *J. Inorg. Nucl. Chem.* **1973**, *35*, 1525−1530. (b) Milman, V.; Winkler, B.; Pickard, C. J. *J. Nucl. Mater.* **2003**, *322*, 165−179.
(7) Sykora, R. E.; Assefa, Z.; Haire, R. G.; Albrecht-Schmitt, T. E. *J. Solid State Chem.* **2004**, *177*, 4413−4419.
(8) Assefa, Z.; Haire, R. G.; Sykora, R. E. *J. Solid State Chem.* **2008**, *181*, 382−391.
(9) Skanthakumar, S.; Antonio, M. R.; Wilson, R. E.; Soderholm, L. *Inorg. Chem.* **2007**, *46*, 3485−3491.
(10) Polinski, M. J.; Wang, S.; Alekseev, E. V.; Depmeier, W.; Albrecht-Schmitt, T. E. *Angew. Chem., Int. Ed.* **2011**, *50*, 8891−8894.
(11) Polinski, M. J.; Wang, S.; Alekseev, E. V.; Depmeier, W.; Liu, G.; Haire, R. G.; Albrecht-Schmitt, T. E. *Angew. Chem., Int. Ed.* **2012**, *51*, 1869−1872.
(12) Diwu, J.; Nelson, A-G. D.; Albrecht-Schmitt, T. E. *Comments Inorg. Chem.* **2010**, *31* (1 & 2), 46−62.
(13) Diwu, J.; Nelson, A.; Wang, S.; Albrecht-Schmitt, T. E. *Inorg. Chem.* **2010**, *49*, 3337−3342.
(14) Diwu, J.; Wang, S.; Liao, Z.; Burns, P. C.; Albrecht-Schmitt, T. E. *Inorg. Chem.* **2010**, *49*, 10074−10080.
(15) Diwu, J.; Wang, S.; Good, J.; Victoria, D.; Albrecht-Schmitt, T. E. *Inorg. Chem.* **2011**, *50*, 4842−4850.
(16) Diwu, J.; Good, J. J.; Di Stefano, V. H.; Albrecht-Schmitt, T. E. *Eur. J. Inorg. Chem.* **2011**, *9*, 1374−1377.
(17) Diwu, J.; Wang, S.; Albrecht-Schmitt, T. E. *Inorg. Chem.* **2012**, *51* (7), 4088−4093.
(18) Sheldrick, G. M. *SADABS, Program for absorption correction using SMART CCD based on the method of Blessing*; University of Göttingen: Göttingen, Germany, 1996. Blessing, R. H. *Acta Crystallogr.* **1995**, *A51*, 33−38.
(19) Sheldrick, G. M. *Acta Crystallogr.* **2008**, *A46*, 112−122.
(20) Hohenberg, P.; Kohn, W. *Phys. Rev.* **1964**, *136*, 864−871.
(21) Kohn, W.; Sham, L. J. *Phys. Rev.* **1965**, *140*, 1133−1138.
(22) Roos, B. O.; Taylor, P. R.; Siegbahn, P. E. M. *Chem. Phys.* **1980**, *48*, 157−173.
(23) Andersson, K.; Malmqvist, P.-Å.; Roos, B. O. *J. Chem. Phys.* **1992**, *96*, 1218−1228.
(24) Perdew, J. P.; Burke, K.; Ernzerhof, M. *Phys. Rev. Lett.* **1996**, *77*, 3865−3868.
(25) Schaefer, A.; Huber, C.; Ahlrichs, R. *J. Chem. Phys.* **1994**, *100*, 5829−5836. Eichkorn, K.; Weigend, F.; Treutler, O.; Ahlrichs, R. *Theor. Chem. Acc.* **1997**, *97*, 119−124.
(26) Cao, X. Y.; Dolg, M. *J. Chem. Phys.* **2001**, *115*, 7348−7356.
(27) Ahlrichs, R.; Bar, M.; Haser, M.; Horn, H.; Kolmel, C. *Chem. Phys. Lett.* **1989**, *162*, 165−169.
(28) Hess, B. A. *Phys. Rev. A* **1986**, *33*, 3742−3748.
(29) Roos, B. O.; Lindh, R.; Malmqvist, P.-Å.; Veryazov, V.; Widmark, P. O. *J. Phys. Chem. A* **2005**, *109*, 6575−6579.
(30) Aquilante, F.; Gagliardi, L.; Pedersen, T. B.; Lindh, R. *J. Chem. Phys.* **2009**, *130*, 154107−154116.
(31) Aquilante, F.; Pedersen, T. B.; Lindh, R.; Roos, B. O.; De Meras, A. S.; Koch, H. *J. Chem. Phys.* **2008**, *129*, 024113−024121.
(32) Aquilante, F.; Malmqvist, P. A.; Pedersen, T. B.; Ghosh, A.; Roos, B. O. *J. Chem. Theory Comput.* **2008**, *4*, 694−702.
(33) Aquilante, F.; Pedersen, T. B.; Lindh, R. *J. Chem. Phys.* **2007**, *126*, 194106−194117.
(34) Gagliardi, L.; Roos, B. O. *Chem. Soc. Rev.* **2007**, *36*, 893−903. Gagliardi, L. *J. Am. Chem. Soc.* **2003**, *125*, 7504−7505.
(35) La Macchia, G.; Brynda, M.; Gagliardi, L. *Angew. Chem., Int. Ed.* **2006**, *45*, 6210−6213.
(36) Gagliardi, L.; Heaven, M. C.; Krogh, J. W.; Roos, B. O. *J. Am. Chem. Soc.* **2005**, *127*, 86−91.
(37) Gagliardi, L.; La Manna, G.; Roos, B. O. *Faraday Discuss.* **2003**, *124*, 63−68.
(38) Grant, D. J.; Stewart, T. J.; Bau, R.; Miller, K. A.; Mason, S. A.; Gutman, M.; McIntyre, G. J.; Gagliardi, L.; Evans, W. J. *Inorg. Chem.* **2012**, *51*, 3613.
(39) Karlström, G.; Lindh, R.; Malmqvist, P.-Å.; Roos, B. O.; Ryde, U.; Veryazov, V.; Widmark, P. -O.; Cossi, M.; Schimmelpfennig, B.; Neogrady, P.; Seijo, L. *Comput. Mater. Sci.* **2003**, *287*, 222−239.
(40) (a) Guillaumont, R.; Desire, B.; Galin, M. *Radiochem. Radioanal. Lett.* **1971**, *8*, 189−198. (b) Diakonov, I. I.; Ragnarsdottir, K. V.; Tagirov, B. R. *Chem. Geol.* **1998**, *151*, 327−347.
(41) Carnall, W. T.; Fields, P. R.; Pappalardo, R. G. *J. Chem. Phys.* **1970**, *53*, 2922−2938.
(42) Pappalardo, R. G.; Carnall, W. T.; Fields, P. R. *J. Chem. Phys.* **1969**, *51*, 1182−1200.